Swimming performance and unique wake topology of the sea hare (*Aplysia*)

Zhuoyu Zhou and Rajat Mittal*
Department of Mechanical Engineering, Johns Hopkins University, Baltimore, Maryland 21218, USA

(Received 25 October 2017; published 16 March 2018)

The *Aplysia*, commonly referred to as the "sea hare," is a marine mollusc that swims using large-amplitude flapping of its wide, winglike parapodia. In this study, flow simulations with a relatively simple kinematical model are used to gain insights into the vortex dynamics, thrust generation, and energetics of locomotion for this animal. A unique vortex pattern characterized by three distinct trains of vortex ringlike structures is observed in the wake of this animal. These vortex rings are associated with a positive momentum flux in the wake that counteracts the drag generated by the body. Simulations indicate propulsive efficiencies of up to 24% and terminal swimming speeds of about 0.9 body length per cycle. Swimming speeds are found to increase with increasing parapodial flapping amplitude as well as wavelength of undulation.

DOI: 10.1103/PhysRevFluids.3.033102

I. INTRODUCTION AND BACKGROUND

All *Aplysia* are benthic gastropods (Phylum Mollusca) and among the 37 recognized species, seven (*A. brasiliana*, *A. depilans*, *A. extraordinaria*, *A. fasciata*, *A. morio*, *A. pulmonica*, and *A. tanzanensis*) are good swimmers [1] that can cross large distances in one swim episode and also maintain a fairly straight path against natural currents. *A. brasiliana* and *A. fasciata* are two related species [2] whose swimming has been investigated in some detail. All species of *Aplysia* swim by flapping of the winglike parapodia [3] that is actuated by a wave of muscle contraction from the anterior to the posterior of each parapodium; the parapodia are folded to cover the mantle area during the upstroke (closing phase) and fully extended to expose the mantle area during the downstroke (opening phase). The amplitude of flapping is typically very large with the two parapodia overlapping at the end of the upstroke.

The simple neural system with large neurons and axons has made the sea hare, or *Aplysia*, a valuable laboratory animal for investigations into the nervous systems and brain function and neuronal control of swimming in these animals [4–6]. Efforts have also been made to study the energetics of locomotion of these animals by evaluating the cost of transport [7]. The propulsive mechanism for the mode of swimming adopted by these animals is, however, still unclear. Proposed mechanisms include sculling, jet propulsion, and hydrodynamic lift [1,7]. Porten *et al.* [5] suggested that the leading edge of the parapodia presents as an "airfoil" that produces lift on both power and recovery strokes. They suggested that while the anterior third of the parapodia produces thrust, the rear two-thirds provides pitch stability during swimming.

In the classification scheme of swimming gaits in marine gastropods put forth by Farmer [3], the *Aplysia* employs paired flapping of its parapodia for swimming. However, in the larger context of swimming animals, we note that the swimming gait of *Aplysia* is most similar to the so-called rajiform and mobuliform modes of propulsion adopted by batoid fish, such as electric rays, sawfishes, guitarfishes, skates, and stingrays [8]. In these modes, thrust is generated by passing a synchronized

*mittal@jhu.edu

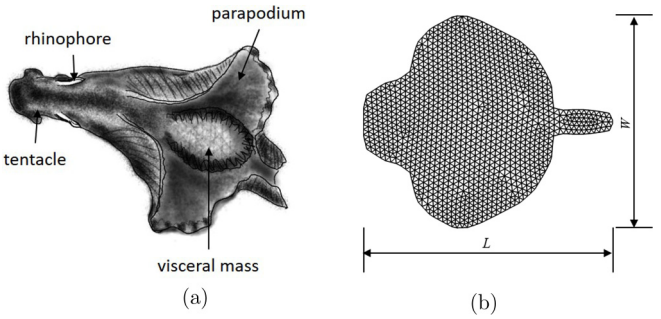

FIG. 1. (a) External features of free-swimming sea hare (*A. fasciata*) in a streamlined posture; (b) the planform used in this study adopted from a dissected *A. brasiliana* with the dorsal visceral mass removed [5].

undulatory traveling wave along the pectoral fins. The feature that distinguishes these two modes is the wave number (number of waves per body length) of the undulatory wave; in the rajiform mode, the wave number is greater than one, whereas in the mobuliform mode, the wave number is less than half. Stingrays swim using the rajiform mode with a mean wave number of about 1.1, whereas fish such as cownose rays (*Rhinoptera bonasus*) are found to have about 0.4 waves on their fins [8]. As we will show later, the *Aplysia* has wavelengths that compare to the mobuliform mode, but the amplitude of flapping in *Aplysia* significantly exceeds anything seen in batoid fishes. It is expected that this exaggerated movement of the parapodia will generate hydrodynamical features that are different from those observed for batoid fish, and this movement and associated hydrodynamics will also impact the swimming performance in ways that has not been elucidated in previous studies of swimming in batoid fish.

The large amplitude movement of the parapodia in *Aplysia* as compared to batoid fish is undoubtedly associated with the absence of a skeleton and other bony or cartilaginous structures in these marine gastropods, which allows significant bending in their appendages and parapodia. This versatility in movement is also one factor that makes these animals attractive for consideration as bioinspired or biohybrid soft robots, and recently, attempts have been made to develop soft-biohybrid robots with both organic actuation and organic motor-pattern control inspired by the locomotion of the nonswimming species *Aplysia californica* [9,10]. Thus, this application in the area of soft robotics generates additional interest in the swimming performance of soft-bodied animals such as *Aplysia*.

In the current study, we employ high-fidelity computational fluid dynamics to model free-swimming in these animals and use the simulation to gain insights into the flow features, propulsive mechanisms, and energetics of locomotion. Simulations are also conducted to explore the effects of variations in kinematics, such as parapodial flapping amplitude and undulatory wavelength. Understanding of the hydrodynamics of these animals may also help in the development of softbodied bioinspired or biohybrid robots that utilize either living neuron, or living tissue, or both to swim [9].

II. METHODS

A. Body geometry and swimming kinematics

The body of *Aplysia* consists of a head, a foot, and a visceral mass. The foot is short posteriorly and forms a pointed tail; it then expands anteriorly into two large, winglike parapodia [see Fig. 1(a)]. Between the two parapodia is the reduced mantle and mantle cavity, in which the shell is embedded and covers the visceral mass. Figure 1(a) shows the external morphology of a free-swimming *A. brasiliana*, with the body in a streamlined posture [11] and the edges of the foot curled inward such that the normal crawling surface is hidden along most of its length.

Because the two thin parapodia dominate the total surface area of the animal and are responsible for most of the hydrodynamics of the locomotion, in the current study, the entire body of the *Aplysia*

is modeled as a zero-thickness deformable membrane. The planform of these animals is adopted from Fig. 7 in Ref. [5] of a dissected *A. brasiliana* with the dorsal visceral mass removed. Bebbington and Hughes [12] described the differences in the shape of the pedal sole and parapodia of three swimming species: *A. depilans*, *A. fasciata*, and *A. punctata*, while the shape of the parapodia varies slightly among species, we consider the flat, distended shape of *A. brasiliana* [see Fig. 1(b)] as a good representation of these animals.

As reported in Ref. [11], when swimming at the surface, the sea hare exhibits a complex swimming gait that combines a head-bobbing with each parapodial flapping, similar to the swimming gaits of the Spanish Dancer (*Hexabranchus sanguineus*). The bobbing movement is, however, usually not observed when swimming below the surface, and this also agrees with the observation by Porten *et al.* [5]. Since these animals are difficult to maintain in laboratory conditions, the kinematics of the body for the current study are obtained from a field video of an animal recorded swimming close to the seabed [13]. In this video, the animal is observed to swim by passing synchronous waves along the two parapodia. The animal moves in a fairly straight path, and this video therefore serves as a suitable basis for modeling linear swimming of these animals. It is worth pointing out that Bebbington and Hughes [12] noted a slight phase difference between the movements of the two parapodia in *A. fasciata*, whereas the measurements of Porten *et al.* [5] indicated little phase difference in flapping. The video of Carletti [13] and our model are in line with the latter study. Therefore, the time-dependent angular deflection of the parapodia with respect to the axis-of-symmetry is described by a synchronized traveling wave as

$$\psi_m(x,y,t) = \tfrac{1}{2}\{1+\tanh[(y-y_0)/K]\}\psi_0 \sin[2\pi(x/\lambda - t/T)],$$
$$0 \leqslant x \leqslant L, -W/2 \leqslant y \leqslant W/2, \tag{1}$$

where ψ_0 is the angular amplitude of the parapodial deflection, x and y are the chordwise and spanwise coordinates, respectively (L and W are the length and width of the body), T is the cycle period. Because the shape of the paired parapodia is bilaterally symmetric, but the movements are asymmetrical with one parapodium closing over the other during the closing phase, the flapping amplitudes of the two sides $\psi_{0,l}$ and $\psi_{0,r}$ (where the subscripts l and r denote the left and right sides, respectively) are prescribed to be slightly different to capture this feature. The hyperbolic tangent function prescribes the spanwise variations with two parameters, K and y_0, both of which have dimensions of length. It should be noted that we do not directly model the flexibility of the body since that requires knowledge of the tissue properties and muscle activation, which is currently lacking. Instead, the flexibility and softness of the body of these animals manifests through the large-scale bending of the parapodia, which we match to actual observations swimming in these animals.

The membrane representing the body is divided into triangular elements where each element is attached to a virtual joint that can rotate about a hinge parallel to the axis-of-symmetry. The locomotion of the swimmer defined by Eq. (1) can then be generated by smoothly rotating these joints following the Denavi-Hartenberg convention [14], which ensures that the total length and area of the body is very nearly conserved. Figure 1(b) shows the distended planform meshed with triangular elements. With the kinematics of the body prescribed about the axis-of-symmetry, simulations are carried out where the acceleration and movement of the body are computed by direct coupling of the Navier-Stokes equations [see Eqs. (2) and (3)] with the body dynamics equations [see Eq. (5)].

The above kinematic model introduces five nondimensional parameters: the flapping amplitudes of the two parapodia $\psi_{0,l}$, $\psi_{0,r}$, the length-specific wavelength λ/L, K/L and y_0/L, where K/L describes the smoothness of the spanwise direction and y_0/L prescribes the location where the flapping angle is half of the maximum value in the spanwise direction respectively. These parameters were initially estimated from selected still frames of the video to achieve a good visual match. The parameters controlling the spanwise variations are chosen as $K/L = 0.1$ and $y_0 = W/4$ for all *Aplysia* models investigated in this study. The other parameters used in our baseline case are $\psi_{0,l} = 97.5^\circ$, $\psi_{0,r} = 165^\circ$, and $\lambda/L = 2.0$. As pointed out earlier, the amplitude of undulation in

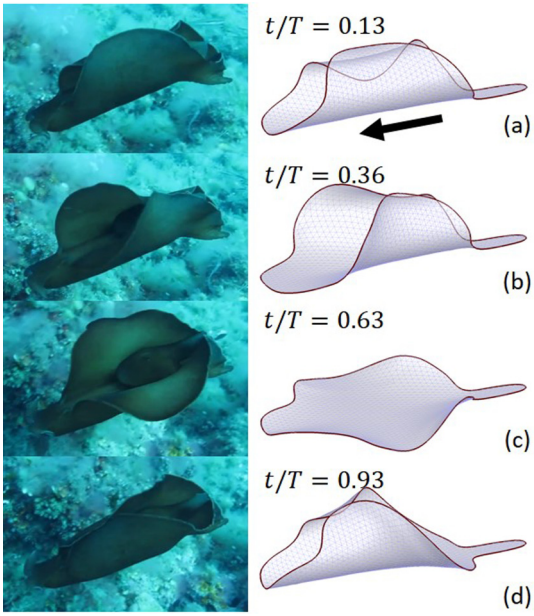

FIG. 2. Comparison of the reconstructed motion of the *Aplysia* with screenshots of a freely swimming *A. fasciata* [13]. (a) Fully closed; (b) beginning of opening phase; (c) fully open; (d) beginning of closing phase. The thick black arrow denotes the direction of swimming.

Aplysia is significantly higher than that observed for batoid fish. For instance, cownose rays (*R. bonasus*), which swim by using the mobuliform mode, exhibit the highest flapping amplitude among the eight species studied by Rosenberger [8]. However, their angular amplitude still only corresponds to about 35° per the current kinematic description, while the peak-to-peak angular amplitude of manta rays has been measured to be about 60° [15]. Thus, the hydrodynamics of swimming in *Aplysia* is expected to be quite distinct from batoid fish. Figure 2 shows four representative stages of the reconstructed swimming structure in comparison with the screenshots of a freely swimming *A. fasciata* from the field video and we note that the reconstruction provides a reasonable match. Quantitative information on the kinematics of free-swimming Aplysia is not available for a more quantitative comparison with the current model.

B. Computational method

We briefly summarize here the approach employed to simulate the coupled flow-body system that has been described in more detail in Ref. [16] and extensively validated against other studies [17,18]. The equations governing the flow are the 3D unsteady Navier-Stokes equations formulated in a noninertial frame that translates with respect to a body-fixed point:

$$\frac{\partial u_i}{\partial x_i} = 0, \tag{2}$$

$$\frac{\partial u_i}{\partial t} + \frac{\partial [u_i(u_j - V_j)]}{\partial x_j} = -\frac{1}{\rho}\frac{\partial p}{\partial x_i} + \nu \frac{\partial}{\partial x_j}\left(\frac{\partial u_i}{\partial x_j}\right), \tag{3}$$

where $i, j = 1,2,3$, u_i is the absolute fluid velocity in the inertial reference frame, V_j is the translational velocity of the reference point on the body, p is the pressure, and ρ and ν are the fluid density and kinematic viscosity, respectively. Simulation in the frame attached to the center-of-mass of the animal's body keeps the model in the central region of the computational

domain through the entire simulation. This reduces the resolution requirements for the simulations and also makes the approach to the terminal swimming state agnostic to the size of the computational domain. Once the flow field is resolved at each time step, the forces acting on the body can be readily computed by integrating the pressure and viscous stress over the surface as follows:

$$\vec{F} = -\int_{\partial B} (-p\hat{n} + \vec{\tau})dS, \tag{4}$$

where ∂B denotes the surface of the body, $\vec{\tau}$ the shear stress acting on the surface, and $\hat{n}$ the unit normal vector pointing out of the fluid control volume.

In this work, the body motion relative to the noninertial frame is prescribed by the kinematic model discussed before. Given the observation that the animal swims along a nearly linear path with one degree of freedom, the body is constrained to swim only along the forward direction (surge), and all sideways (sway) and vertical (heave) movements as well as any flow-induced rolling, yawing, and pitching motion of the body are neglected.

In reality, the flapping motion of these animals likely generates lateral and vertical forces as well as hydrodynamic torques, and the animal makes continuous compensatory adjustments to its movements to swim straight without drifting upwards and sideways or rolling, pitching, or yawing. These adjustments are difficult to include in the computational model, and here we assume that these collateral forces and torques are small compared to the forces in the surge direction and neglect these other degrees-of-freedom altogether. Later in the paper, we evaluate this assumption using our computations. With the hydrodynamic force computed as above, the forward velocity of the body is estimated by solving Newton's second law for the animal,

$$\rho_b S \frac{dV}{dt} = F, \tag{5}$$

where ρ_b is the area density of the body, which is derived from the measurements of *A. brasiliana* [7], S is the planar area of the animal. Thus, the above fluid-structure interaction problem is solved in a coupled but sequential manner. For an animal with a parapodial area of 50 cm^2, the area density is about 20 kg/m^2, and this is the value used in the current study. This leads to a nondimensional density ratio ($\rho_b/L\rho$) equal to 0.2.

C. Simulation setup

As discussed in Ref. [16], the hydrodynamics and swimming performance of the animal can be fully determined by the geometric and kinematic parameters, as well as the density ratio, and the Stokes number $\Sigma = 2\pi f L A_m/\nu$, where f is the flapping frequency, L is the body length, A_m is the flapping amplitude. The Stokes number can also be interpreted as Reynolds number based on flapping velocity of the parapodia. Statistical analysis [7] of 25 fully grown specimens, with live body mass ranging from 34 to 506 g and the corresponding parapodial area (single parapodium) from about 20 to 200 cm^2, indicates Stokes numbers from $O(10^4)$ to $O(10^5)$ for the swimming of these animals. In the current study, we choose a nominal value of $\Sigma = 3450$, which is high enough to be representative of these animals, but low enough to allow adequate resolution of the flow features and vortices. For context, this Stokes number could represent an *Aplysia* of parapodial area (single parapodium only) of 25 cm^2.

The computational domain used in this study is of size $10L \times 8L \times 7L$ and the head of the *Aplysia* is placed at $(3L, 4L, 3.5L)$. The configuration is chosen such that the domain is large enough so that the outer boundary can be considered nearly undisturbed, and far-field (Neumann) boundary conditions are applied for both pressure and velocity on all the outer boundaries. A systematic grid refinement study (described in the Appendix) was carried out for an animal swimming in a uniform inflow, and a grid with 7.5 million grid points ($301 \times 193 \times 129$) and a time step of $0.002T$ [corresponding to a mean Courant-Friedrichs-Lewy (CFL) number of about 0.5] was chosen for the final simulations.

III. RESULTS

Simulation results of free-swimming *Aplysia* are presented in this section. For all simulations, animals are initially released in a stationary fluid, and as the flapping ensues, the animals accelerate and eventually reach a quasisteady terminal swimming state. In all cases, it takes about eight cycles to reach this quasi-steady state and simulations are continued for about five additional cycles to accumulate statistics.

A. Metrics for assessing swimming performance and flow characteristics

The 3D wake structure generated by the self-propelled swimmers are identified by the Q-criterion [19], the quantity Q is defined as $Q = \frac{1}{2}(||\boldsymbol{\Omega}||^2 - ||\boldsymbol{S}||^2)$, where $\boldsymbol{\Omega}$ and $\boldsymbol{S}$ are the antisymmetric and symmetric parts of the velocity gradient tensor $\nabla\vec{u}$, respectively. A vortex is defined as a region where the rotational motion dominates the rate-of-strain and $Q > 0$. Vortices are visualized by plotting isosurfaces of Q values.

The forward swimming speed V is nondimensionalized as $V^* = VT/L$ and this can be viewed as the number of body-length traveled per cycle [16]. The force coefficient in the surge direction is computed as

$$C_s = \frac{F^{\text{surge}}}{\frac{1}{2}\rho \bar{V}_T^2 S}, \tag{6}$$

where S is the planar area of the body, and F^{surge} is the force component along the surge direction, $\bar{V}_T$ is the mean terminal swimming speed, with the terminal condition defined to be when the variations of the cycle-averaged swimming velocity is within 3%.

The Froude propulsive efficiency is estimated for the quasisteady state, when the cycle-averaged thrust is exactly balanced by the cycle-averaged drag force, and it is computed as

$$\eta_f = \frac{W_{\text{useful}}}{W_{\text{total}}} = \frac{1}{T\bar{P}_{\text{total}}} \int_0^T \left[\sum_{k=1}^{N} \left(\frac{F_k^{\text{surge}}(t) + |F_k^{\text{surge}}(t)|}{2} \right) U_k^{\text{surge}}(t) \right] dt, \tag{7}$$

where $\bar{P}_{\text{total}} = \int_0^T \sum_{k=1}^{N} \vec{F}_k(t) \cdot \vec{U}_k(t) dt$ is the total expended power, N is the total number of triangular elements on the surface, k is the element index, $\vec{U}_k$ is the element velocity, U_k^{surge} is the forward velocity of each element, $\vec{F}_k = (F_k^{\text{surge}}, F_k^{\text{sway}}, F_k^{\text{heave}})$ is the force exerted by each triangular element on the surrounding fluid, and T is the cycle period. The above definition of Froude efficiency applies to all modes of swimming and makes use of the ability in computational fluid dynamic simulations, to separate thrust and drag generating elements of the body in space and time. This same methodology has been used before to estimate the Froude efficiency of undulatory propulsion in humans [20] and cetaceans [20], carangiform swimming in fish [21] and swimming in other marine gastropods [16]. Following Schultz and Webb [22], we also compute a power (or equivalently, an effective swimming drag) coefficient for the terminal state as

$$\bar{C}_P = \frac{\bar{P}_{\text{total}}}{\frac{1}{2}\rho \bar{V}_T^3 S} = \frac{\bar{D}_{\text{effective}}}{\frac{1}{2}\rho \bar{V}_T^2 S}, \tag{8}$$

where $\bar{C}_P$ is the power (or equivalently, the effective drag) coefficient and $\bar{D}_{\text{effective}} = \bar{C}_P / \bar{V}_T$ is the effective drag force of the swimming body.

B. Wake topology

In this section, we focus on the vortex wake of a self-propelled Aplysia. We describe here the wake topology for the baseline case with $\lambda/L = 2.0$ only because the key features do not vary much with the kinematic parameters studied here. Figure 3 shows the vortex structures for the terminal swimming condition. In this plot, we identify three sets of vortex rings (curved arrows) in the wake, with a

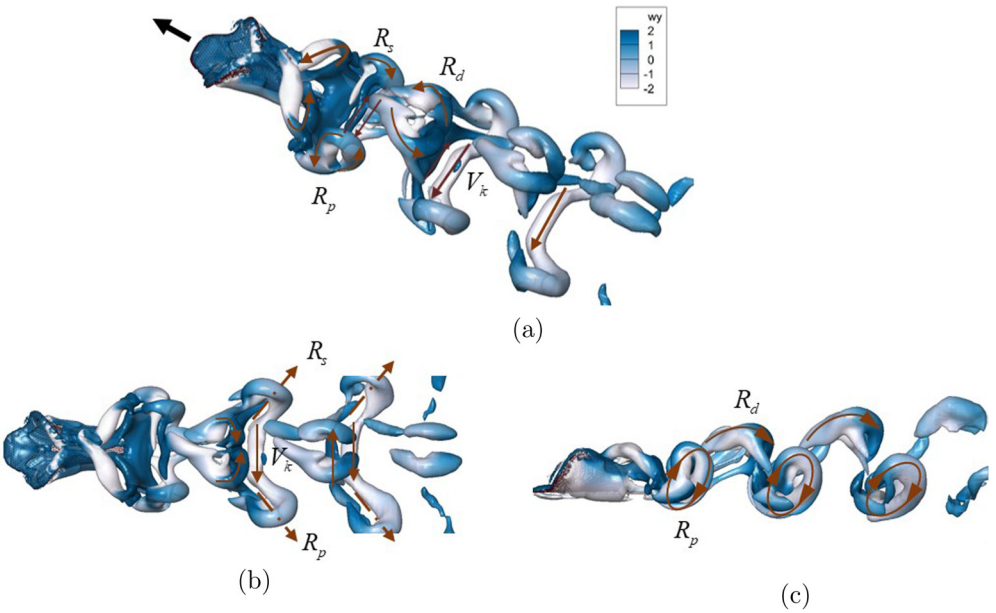

FIG. 3. Vortex topology for the baseline case $\lambda/L = 2.0$: (a) perspective view; (b) dorsal view; (c) side view. The visualized vortex structures corresponding to the isosurface of $Q = 2.0$ are colored by vorticity in the spanwise direction. The thick arrow denotes the direction of swimming and the other arrows depict the direction of rotation of these vortices.

pair of vortex rings (R_s and R_p) oriented in the spanwise direction and connected by two horizontal vortices (straight solid arrows), and a third set of vortex rings (R_d) orientated along the streamwise direction. The dash-dot arrows denote the orientation of these vortex rings. A close examination of the vortex formation process indicates that while the vortex rings R_s and R_p are generated by the downstroke of the caudal tip of the parapodia, the dorsal vortex ring R_d is generated by the upstroke of the parapodia at the caudal end. With respect to this dorsal vortex wake, the upstroke actually generates two vortex loops at the parapodia tips that have the same azimuthal rotation; these two vortex loops are ejected into the wake at the beginning of the downstroke and rapidly approach each other as they convect downstream in the near wake and nearly coalesce into an identifiable vortex ring.

A comparison of this wake with those of flapping foils (Fig. 8 in Dong *et al.* [23]) and other swimmers (Figs. 8 and 10 in Ref. [25]; Fig. 13 in Ref. [15]) provides a useful context for interpreting the current results. The paired vortex rings on the port and starboard side of the animal (R_p and R_s, respectively) produced by parapodial undulation resemble the oblique vortex rings shedding by a finite-aspect ratio flapping foil [23], as well as the linked vortex rings of freely swimming eels (anguilliform), mackerel (subcarangiform), and manta rays (rajiform), all of which present two, and only two sets of vortex rings [15,24,25]. Despite these similarities, the paired vortex rings of *Aplysia*, are shed simultaneously in a nonstaggered pattern at the parapodia tips while the vortex rings from these other foils and swimmers are shed alternately from the two ends and arrange in a staggered fashion.

A more interesting feature that distinguishes the current observed wake pattern from those previously reported, especially as compared to batoid fish, is the formation of the third distinct train of vortex rings (R_d) that is arranged along the dorsal end of the wake. There is little similarity between the vortex topology of these *Aplysia* and that of rajiform or mobuliform swimmers such as rays, skates [26], and mantas [15]. In Ref. [15], flow simulations of a manta ray at Reynolds numbers

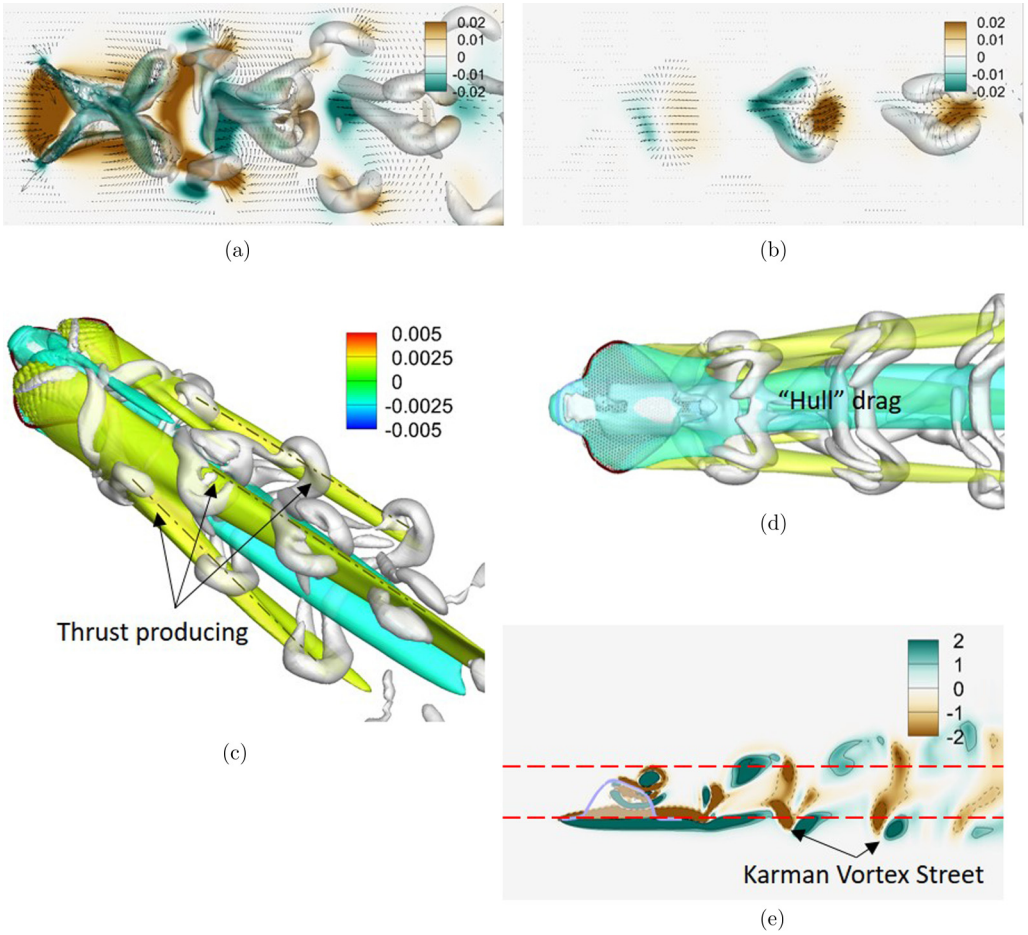

FIG. 4. Correlation between vortex structures, induced velocity and momentum flux in the wake for the baseline case $\lambda/L = 2.0$ at the terminal condition: (a) top-view slice intersecting the paired vortex rings (R_p and R_s); (b) slice intersecting the top set of vortex rings (R_d), the colored contours are the streamwise momentum flux ($u|u|$); (c) perspective view of isosurfaces of ($u|u|$) superposed on vortex structures; (d) ventral view of (c); (e) spanwise vorticity on the symmetry plane, red dashed lines indicate the sliced location of (a) and (b).

comparable to the current case were conducted and the simulation (Fig. 19 of the paper) showed the formation of two pairs of vortex loops for one full stroke. These vortex loops were observed to arrange in a wake that expands in the dorsoventral direction, but not in the lateral direction. The *Aplysia*, on the other hand, forms a pair of laterally arranged vortices at the end of the downstroke and a single, dorsally arranged vortex loop due to the coordinated upstroke of the parapodia. This wake is seen to expand both in the lateral direction as well as the dorsoventral direction. Finally, the wake also contains a vortex street composed of pairs of counter-rotating vortices identified in Fig. 3(a) as V_k that are aligned along the spanwise direction and connect the laterally arranged vortex rings in the near wake.

The correlation between the vortex structures and the thrust production is elucidated in Fig. 4. We pick two slices intersecting the centers of the laterally paired vortex rings and the dorsal vortex rings, respectively. Figures 4(a) and 4(b) show 2D slices selected from the dorsal view. In these plots, the vortex structures are illustrated in grayscale, and velocity vectors are superposed onto the contours

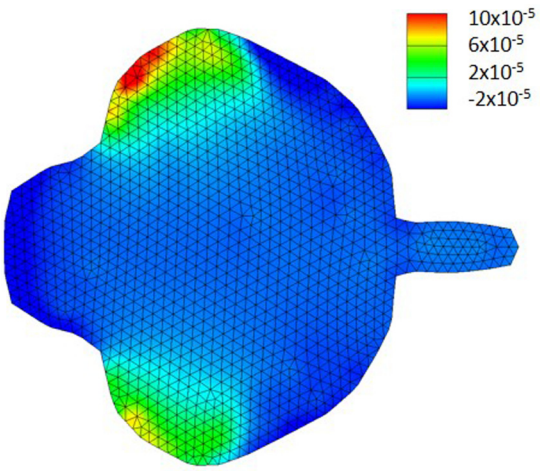

FIG. 5. Cycle-averaged streamwise force coefficient per unit area on the body for the baseline case $\lambda/L = 2.0$, higher curvature in the right parapodium leads to higher thrust.

of $(u|u|)$, which is indicative of the streamwise momentum flux induced by the vortices. It can be seen that the dorsal vortex rings induce strong downstream (positive in the current convection) oriented momentum flux, which signifies thrust generation. Combining this with the observation that a pulsatile jet in the streamwise direction would create a set of vortex rings similar to those seen along the wake centerline here, we reach the conclusion that the notion of jet propulsion as a contributory mechanism for swimming in these animals [1,7] has some merits. We also note that the two horizontal (spanwise) vortices behind the body center that connect the paired vortex rings, contribute an upstream (negative) oriented momentum flux and this can be viewed as the 'hull' drag caused by the body. Thus, all three sets of vortex rings are thrust producing, whereas the horizontally oriented vortices are drag inducing.

We further examine this correlation by superimposing the isosurfaces of $(u|u|)$ onto the isosurfaces of the vortex structures as presented in Figs. 4(c) (perspective view) and 4(d) (ventral view). The three streaks of positive streamwise momentum flux are found to be precisely located along the centers of the three sets of vortex rings, confirming that the vortex rings are indeed the sources of thrust. The negative momentum flux associated with the 'hull' drag of the animal, however, is located between the two horizontal vortices as observed from the ventral view in Fig. 4(d). By plotting the spanwise vorticity on the symmetry plane [Fig. 4(e)], these horizontal (spanwise) vortices are found to resemble a Karman vortex street that is associated with drag generation. Thus, the self-propelled *Aplysia* produces a wake that shows a clear spatial separation in thrust and drag.

Figure 4 makes it clear that the vortex rings are generated by parapodial flapping, whereas the drag-based spanwise vortices (identified as V_k) are shed behind the nondeforming portion of the body. This implies that the two parapodia act as the "propellers," while the rest of the body acts as the "hull." Figure 5 shows the cycle-averaged streamwise force per unit area on the body. It can be readily seen from this figure that the anterior portion of the parapodia generates most of the thrust, whereas the rest of the body generates drag on average. This confirms the hypothesis [5] that the leading edge of parapodia generates most of the thrust. We note that the asymmetry in the streamwise force distribution on the parapodia, as well as in the isosurfaces of momentum flux and vortex structures, results from the asymmetry in the flapping motion.

C. Effects of kinematic parameters on swimming performance

As mentioned earlier, the amplitude of the parapodia undulation is found to vary significantly for these animals, with energetic swimmers showing overlapped (and therefore high-amplitude) flapping,

TABLE I. Kinematic parameters employed in modeling the swimming of *Aplysia* and the corresponding swimming performance.

Case	$\psi_{0,l}$	$\psi_{0,r}$	λ/L	$\bar{V}_T^*$	η_f	$\bar{C}_P$
Baseline	97.5°	165°	2.0	0.81	23.8	0.96
C1	97.5°	165°	3.3	0.89	20.6	1.00
C2	97.5°	165°	1.5	0.65	22.7	1.28
C3	90°	90°	2.0	0.75	22.6	1.04
C4	90°	90°	1.0	0.45	19.2	2.14
C5	75°	75°	2.0	0.65	21.3	1.10
C6	75°	75°	1.0	0.42	22.7	1.94

and tired animals not able to overlap the two parapodia during the flapping [7]. Furthermore, our observation of the kinematics suggests an undulation wavelength of $\lambda/L \leqslant 1$, and the baseline kinematic model of $\lambda/L = 0.5$ shows fair agreement with the video. A quantitative analysis of the effect of parapodial wavelength on swimming performance, which might be interesting from the viewpoint of bioinspired robotics, is not available. We have therefore conducted simulations to explore the effects of both the undulatory amplitude and wavelength on the swimming performance and results from this study are presented in this section.

Table I summarizes the kinematic parameters for the various cases investigated here along with the metrics for swimming performance obtained from the simulations. To provide some context, the baseline case with the highest flapping amplitudes $\psi_{0,l} = 97.5°$ and $\psi_{0,r} = 165°$, as well as cases C1 and C2, as discussed in the kinematic modeling section, correspond to the scenario where the left parapodium closes over the right, and thus, mimics active swimmers; cases C3 and C4 with the intermediate flapping amplitudes $\psi_{0,l} = \psi_{0,r} = 90°$ correspond to the scenario where the two parapodia barely touch each other at the top of the upstroke; in cases C5 and C6 with the lowest flapping amplitudes $\psi_{0,l} = \psi_{0,r} = 75°$, the parapodia are far apart and these could model "tired" swimmers [7]. Figure 6 shows the three representative postures during the closing phase.

Figure 7 shows the temporal variations in swimming velocities and force coefficients in the streamwise direction. The animal is initially released in still fluid; as swimming movements generate hydrodynamic thrust, the animal accelerates and the drag force also increases. The velocity continues to increase until the cycle-averaged streamwise force becomes zero. The nondimensional mean terminal velocities and Froude efficiencies are listed in Table I. Comparison reveals that the mean terminal swimming speed increases with both flapping amplitudes and wavelength. The swimming speeds in the current simulations range from 0.42 to 0.89 body length per cycle, whereas the propulsive

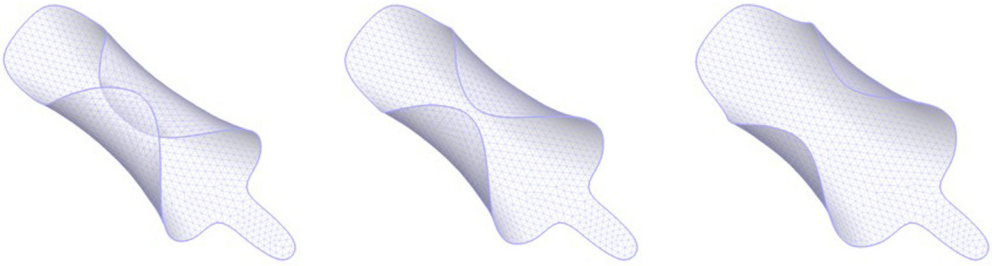

(a) (b) (c)

FIG. 6. Representative kinematic models at the closing phase with wavelength $\lambda/L = 2.0$: (a) Baseline case, $\psi_{0,l} = 97.5°$ and $\psi_{0,r} = 165°$; (b) C3, $\psi_{0,l} = \psi_{0,r} = 90°$; (c) C5, $\psi_{0,l} = \psi_{0,r} = 75°$. Arrow denotes the swimming direction.

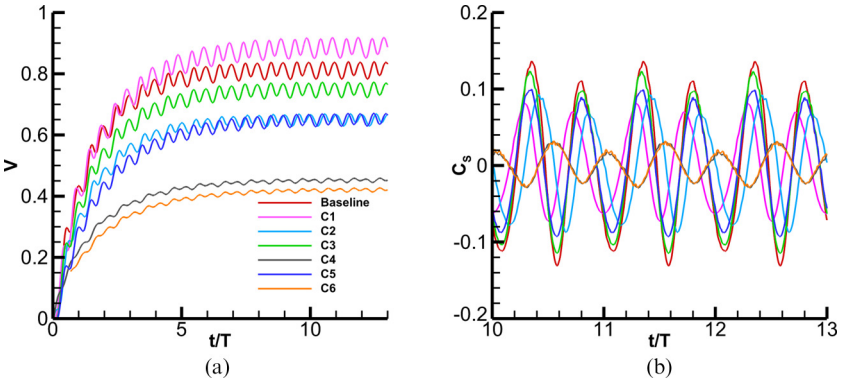

FIG. 7. Comparison of the time history of (a) swimming speed and (b) surge force coefficients for the kinematic parameters investigated in the current study.

efficiencies are about 20% and do not vary much among all cases studied in this work. Therefore, the baseline case that models the kinematics observed from the video is found to have the highest efficiency and a relatively high swimming speed (about 8% less than the highest speed). In contrast, cases C4 and C6 representing "tired" animals have the lowest swimming speed and relatively lower propulsive efficiency as well. Experimental measurements [7] show that the velocity of freshly rested animals is $0.096 \pm 0.014\,\mathrm{m\,s^{-1}}$ (initial speed), and it drops to $0.067 \pm 0.014\,\mathrm{m\,s^{-1}}$ (final speed) after four hours of continuous swimming. For an animal of 10 cm length, as the scale studied in this work, these speeds are equivalent to about 0.1 and $0.7\,\mathrm{BL\,s^{-1}}$, respectively. Thus, our simulation results are quite comparable to the experimental results.

Swimming speeds vary significantly among vertebrate and invertebrate swimming animals. As reported by Tytell and Lauder [27], the speeds of eels range from 0.5 to $2\,\mathrm{BL\,s^{-1}}$. Thus, the swimming speeds of *Aplysia* fall in a range comparable to eels, which employ the so-called anguilliform mode of propulsion. The highest speed of *Aplysia* does not match that of the manta ray, a rajiform swimmer, which can swim at $1.5\,\mathrm{BL\,s^{-1}}$ [15]. For stingrays, Bottom *et al.* [28] reported swimming speeds between 1.5 and $2.5\,\mathrm{BL\,s^{-1}}$, which are significantly faster than the *Aplysia*. *Aplysia* also cannot match the speeds of fish, such as salmon, parrotfish and triggerfish, which easily exceed $3.0\,\mathrm{BL\,s^{-1}}$ [29,30]. Interestingly, the *Aplysia* is also found to underperform in terms of speed of swimming compared to a closely related species of marine gastropods, the Spanish Dancer (*Hexabranchus sanguineus*). This other nudibranch swims with a complex gait that combines dorsoventral body undulation with a bilaterally synchronous, large amplitude progressive wave that passes down its mantle, and recent simulations [16] have provided estimates for terminal speed of 1.33 BL/cycle for these animals.

Comparison of swimming efficiencies are more difficult due to the ambiguity of defining efficiency for an animal swimming at a terminal speed [22]. For instance, the Froude efficiency of eels calculated based on the wake power estimation [27,31], is around 50%. For manta rays, the efficiency evaluated by employing Tytell and Lauder's expression is about 48% [15]. On the other hand, Bottom *et al.* [28] estimated the Froude efficiency (as defined in [27]) of stingrays with fast swimming velocity of $2.5\,\mathrm{BL\,s^{-1}}$ to be 34.1% and slow swimming velocity of $1.5\,\mathrm{BL\,s^{-1}}$ to be 22.9%. An easier comparison of *Aplysia*'s swimming efficiency is to animals for which the swimming efficiency has been calculated using the same expression as in the current paper. Loebbecke *et al.* [20] estimated the swimming efficiency of a cetacean using the same numerical method and same definition of efficiency to be 56% method. For a Spanish Dancer, a species closely related to *Aplysia*, the efficiency for an animal of comparable scale was also estimated to be 57% [16]. Thus, *Aplysia* seems to lag both in terms of swimming speed and efficiency compared to other swimming animals. However, it would seem that the reduction in swimming performance comes with the benefit of decreased kinematic complexity,

especially when compared to the Spanish Dancer, and this might have implications for design of swimming softbodied robots that inspired these marine gastropods. In closing, it should be pointed out that the swimming speed and swimming efficiency of elite, Olympic level swimmers performing the underwater dolphin kick is found to be 0.47 BL s^{-1} and 29%, respectively [20]. Thus, the *Aplysia*, with its simple neuromuscular control system, still manages to outperform the best human swimmers.

Finally, we examine our assumption that the surge force dominates the swimming dynamics of these models. As per Table I, the effective drag coefficient of these swimming animals is O(1). In comparison, the computed mean lateral and vertical force coefficients (nondimensionalized similar to $D_{\text{effective}}$) for these models are approximately 2×10^{-4} and 6×10^{-3}, respectively. Furthermore, the hydrodynamic torques, divided by the characteristic body length, also range from 2×10^{-4} to 6×10^{-3}. Thus, it is reasonable here to neglect these collateral degrees-of-freedom.

IV. CONCLUSIONS

Simulations have been conducted to explore the wake characteristics and swimming performance of the *Aplysia*. The unique wake generated by self-propelled *Aplysia* consists of two sets of vortex rings that extend obliquely away from a centerline in a horizontal plane and another set of vortex rings that extends away in the dorsal direction in the wake. Analysis of the wake shows that the thrust and drag signature of the wake structures is distinct, with the three sets of vortex rings generating thrust and a Karman vortex wake generated by the flow over the body of the animals that is associated with drag. Analysis of the swimming performance indicates that the baseline case, with kinematics chosen to match the field video, is able to obtain the highest propulsive efficiency and a relatively high swimming speed. The overall swimming performance in terms of swimming speed and efficiency, however, seems to lag behind other swimming animals, including the Spanish dancer, which is a closely related species. Given that these animals are soft-bodied invertebrates that have a simple neuromuscular system and live successfully in an environment subject to large changes in both temperature and salinity, they could serve as inspiration for the design of simple, robust and versatile, bioinspired and biohybrid soft swimming robots [10]. We note that, as the muscle forces of these animals are unknown, prescribed kinematics were used for all simulations performed in this study, and the flexibility and softness of the body were not considered.

ACKNOWLEDGMENTS

The authors are very grateful to Simone Carletti, Matteo Charlie Ichino, and George Skeparnias for giving us permission to use their videos of swimming *Aplysia*, and Kuan Xing for making the sketch in

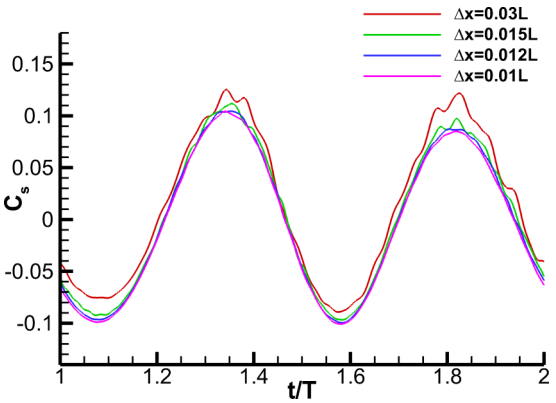

FIG. 8. Temporal profile of surge force coefficients for four grid sizes of an animal swimming in a uniform inflow with the same prescribed kinematics of the case C5.

TABLE II. Mean surge force coefficients and root-mean-square values for various grid sizes.

Δx	$0.03L$	$0.015L$	$0.012L$ (nominal)	$0.01L$
$\bar{C}_s$	0.013	0.002	−0.002	−0.004
$(C_s)_{\text{rms}}$	0.072	0.069	0.069	0.069

Fig. 1(a). Thanks also go to Drs. Jung Hee Seo and Kourosh Shoele for valuable discussions. Support from NSF Grant No. PLR-1246317 is acknowledged. The flow solver developed here benefited from support from NSF Grants No. CBET-1511200 and No. IIS-1344772, and the JHU Provost Discovery Award.

APPENDIX: GRID REFINEMENT STUDY

Grids in this refinement study had a high-resolution region of size $2.5L \times 1L \times 0.6L$ with uniform grid spacing of $0.03L$, $0.015L$, $0.012L$, and $0.01L$ within a computational domain of size $10L \times 8L \times 7L$, with corresponding total grid points of 0.8, 3.0, 7.5, and 9.0 million, respectively. The force coefficients were examined to assess grid dependency and as shown in Fig. 8 the temporal profile of the nominal grid $0.012L$ shows good agreement with the finest grid spacing of $0.01L$. Table II summarizes the key hydrodynamic quantities for this grid refinement study and it's found the difference of both the mean surge force coefficients $\bar{C}_s$ and their root-mean-square (rms) values $(C_s)_{\text{rms}}$ between the nominal and fine grids is within 1%.

[1] T. H. Carefoot, *Aplysia*: Its biology and ecology, Oceanogr. Mar. Biol. **25**, 167 (1987).
[2] M. Medina, T. M. Collins, and P. J. Walsh, mtDNA ribosomal gene phylogeny of sea hares in the genus *Aplysia* (gastropoda, opisthobranchia, anaspidea): Implications for comparative neurobiology, Syst. Biol. **50**, 676 (2001).
[3] W. Farmer, Swimming gastropods (opisthobranchia and prosobranchia), Veliger **13**, 73 (1970).
[4] D. R. McPherson and J. E. Blankenship, Neural control of swimming in *Aplysia brasiliana*. II. Organization of pedal motoneurons and parapodial motor fields, J. Neurophysiol. **66**, 1352 (1991).
[5] K. von der Porten, D. W. Parsons, B. S. Rothman, and H. Pinsker, Swimming in *Aplysia brasiliana*: Analysis of behavior and neuronal pathways, Behav. Neural. Biol. **36**, 1 (1982).
[6] K. von der Porten, G. Redmann, B. Rothman, and H. Pinsker, Neuroethological studies of freely swimming *Aplysia brasiliana*, J. Exp. Biol. **84**, 245 (1980).
[7] D. A. Donovan, S. C. Pennings, and T. H. Carefoot, Swimming in the sea hare *Aplysia brasiliana*: Cost of transport, parapodial morphometry, and swimming behavior, J. Exp. Mar. Biol. Ecol. **328**, 76 (2006).
[8] L. J. Rosenberger, Pectoral fin locomotion in batoid fishes: Undulation versus oscillation, J. Exp. Biol. **204**, 379 (2001).
[9] V. A. Webster, K. J. Chapin, E. L. Hawley, J. M. Patel, O. Akkus, H. J. Chiel, and R. D. Quinn, *Aplysia californica* as a novel source of material for biohybrid robots and organic machines, in *Proceedings of the Conference on Biomimetic and Biohybrid Systems* (Springer, Berlin, 2016), pp. 365–374.
[10] V. A. Webster, F. R. Young, J. M. Patel, G. N. Scariano, O. Akkus, U. A. Gurkan, H. J. Chiel, and R. D. Quinn, 3D-printed biohybrid robots powered by neuromuscular tissue circuits from *Aplysia californica*, in *Proceedings of the Conference on Biomimetic and Biohybrid Systems* (Springer, Berlin, 2017), pp. 475–486.
[11] T. H. Carefoot and S. C. Pennings, Influence of proximal stimuli on swimming in the sea hare, *Aplysia brasiliana*, J. Exp. Mar. Biol. Ecol. **288**, 223 (2003).

[12] A. Bebbington and G. Hughes, Locomotion in *Aplysia* (gastropoda, opisthobranchia), J. Mollus Stud. **40**, 399 (1973).
[13] S. Carletti, *Aplysia fasciata* (2011), https://www.youtube.com/watch?v=K2FQZ7dqgeY.
[14] R. Jazar, Forward kinematics, in *Theory of Applied Robotic: Kinematics, Dynamics, and Control* (Springer Science & Business Media, Berlin, 2010).
[15] F. E. Fish, C. M. Schreiber, K. W. Moored, G. Liu, H. Dong, and H. Bart-Smith, Hydrodynamic performance of aquatic flapping: Efficiency of underwater flight in the manta, Aerospace **3**, 20 (2016).
[16] Z. Zhou and R. Mittal, Swimming without a spine: Computational modeling and analysis of the swimming hydrodynamics of the Spanish Dancer, Bioinspir. Biomim. **13**, 015001 (2018).
[17] D. Kim and H. Choi, Immersed boundary method for flow around an arbitrarily moving body, J. Comput. Phys. **212**, 662 (2006).
[18] N. Mordant and J.-F. Pinton, Velocity measurement of a settling sphere, Eur. Phys. J. B **18**, 343 (2000).
[19] R. Cucitore, M. Quadrio, and A. Baron, On the effectiveness and limitations of local criteria for the identification of a vortex, Eur. J. Mech. B-Fluid. **18**, 261 (1999).
[20] A. von Loebbecke, R. Mittal, F. Fish, and R. Mark, Propulsive efficiency of the underwater dolphin kick in humans, J. Biomech. Eng. **131**, 054504 (2009).
[21] M. Bergmann, A. Iollo, and R. Mittal, Effect of caudal fin flexibility on the propulsive efficiency of a fish-like swimmer, Bioinspir. Biomim. **9**, 046001 (2014).
[22] W. W. Schultz and P. W. Webb, Power requirements of swimming: Do new methods resolve old questions? Integr. Comp. Biol. **42**, 1018 (2002).
[23] H. Dong, R. Mittal, and F. Najjar, Wake topology and hydrodynamic performance of low-aspect-ratio flapping foils, J. Fluid. Mech. **566**, 309 (2006).
[24] I. Borazjani and F. Sotiropoulos, Numerical investigation of the hydrodynamics of carangiform swimming in the transitional and inertial flow regimes, J. Exp. Biol. **211**, 1541 (2008).
[25] G. V. Lauder and E. D. Tytell, Hydrodynamics of undulatory propulsion, Fish Physiol. **23**, 425 (2005).
[26] R. P. Clark and A. J. Smits, Thrust production and wake structure of a batoid-inspired oscillating fin, J. Fluid. Mech. **562**, 415 (2006).
[27] E. D. Tytell and G. V. Lauder, The hydrodynamics of eel swimming, J. Exp. Biol. **207**, 1825 (2004).
[28] R. Bottom II, I. Borazjani, E. Blevins, and G. Lauder, Hydrodynamics of swimming in stingrays: Numerical simulations and the role of the leading-edge vortex, J. Fluid. Mech. **788**, 407 (2016).
[29] S. Cotterell and C. Wardle, Endurance swimming of diploid and triploid atlantic salmon, J. Fish Biol. **65**, 55 (2004).
[30] K. E. Korsmeyer, J. F. Steffensen, and J. Herskin, Energetics of median and paired fin swimming, body and caudal fin swimming, and gait transition in parrotfish (*Scarus schlegeli*) and triggerfish (*Rhinecanthus aculeatus)*, J. Exp. Biol. **205**, 1253 (2002).
[31] E. D. Tytell, The hydrodynamics of eel swimming II. Effect of swimming speed, J. Exp. Biol. **207**, 3265 (2004).